

Using “Heat Tagging” to Understand the Remote Influence of Atmospheric Diabatic Heating through Long-Range Transport

ROBERT FAJBER^a AND PAUL J. KUSHNER^a

^a *Department of Physics, University of Toronto, Toronto, Ontario, Canada*

(Manuscript received 30 September 2020, in final form 19 February 2021)

ABSTRACT: In the circulating atmosphere, diabatic heating influences the potential temperature content of air masses far from where the heating occurs. Budgets that balance local diabatic sources with local heat divergence and storage do not retain information about this remote influence, which requires airmass tracking. In this study, a process-based, passive-tracer diagnostic, called *heat tagging*, is introduced. Heat tagging locally decomposes the potential temperature into contributions from the distinctive diabatic processes that generate them, wherever they occur. The distribution, variability, and transport of atmospheric heat tags are studied in the relatively simple setting of an idealized aquaplanet model. Heat tags from latent heating are generated in the deep tropics and the midlatitude storm track and then transported throughout the troposphere. By contrast, dry sensible heat tags are enhanced near the surface, and radiative tags are mainly confined to the stratosphere. As a result, local heat transport, variability of potential temperature, and global poleward heat transport are dominated by heat tags related to latent heating, with heat tags from sensible and radiative heating only making contributions in the polar near-surface and the stratosphere, respectively. Heat tagging thus quantifies how water vapor and latent heating link the structural characteristics of the atmosphere and illustrates the importance of the hydrological cycle in poleward energy transport.

KEYWORDS: Atmospheric circulation; Energy transport; Mass fluxes/transport; Diabatic heating; Tracers; Global transport modeling

1. Introduction

How do we assess the remote effects of diabatic processes on the atmosphere’s heat content and thermal structure? Diabatic heating must be locally balanced by transport in the climatological mean (Peixoto and Oort 1992), but this does not provide information about remote diabatic heating. Those air masses warmed by tropical convection and condensation in the midlatitude storm tracks are ultimately cooled by longwave emission, which is spread throughout the troposphere (Peixoto and Oort 1992; Ling and Zhang 2013; Zhang et al. 2017). However, how these air masses are transported from regions of heating to regions of cooling, and how each air mass contributes to the thermal structure of the atmosphere requires additional information, necessitating tracking which processes warm air masses and the air masses’ history as they are transported from their regions of generation.

An example of the type of problem that we are interested in studying is how convection influences polar heat content. Inspection of the diabatic heating rates shows that the majority of convection is confined to the deep tropics (Ling and Zhang 2013); are convectively warmed air masses transported from the tropics to the poles and then cool there, or do they cool elsewhere? How does their evolution compare to those air masses warmed through surface heat fluxes in the tropics? Such questions cannot be addressed solely with knowledge

of heating rates since they are inextricably bound to the details of long-range transport and the global circulation.

Tracking the transport of air masses generated by specific diabatic processes is not possible by classical thermodynamic analysis. For example, although comparing the potential temperature and equivalent potential temperature can reveal aspects of the role of latent heat release (Pauluis et al. 2008, 2010; Fajber et al. 2018), such a comparison cannot partition how much heat content originally came from latent heating, because latent heating contributions are inseparable from other diabatic heat sources.

Our goal in this study is to quantify the contributions from different sources of diabatic heating on the thermal structure of the atmosphere in the presence of long-range transport. We do this by using a set of tracers, referred to as “heat tags,” that serve to decompose the potential temperature field into separate contributions from different sources of diabatic heating. The heat tags are added whenever the atmosphere is heated, removed whenever the atmosphere is cooled, and otherwise transported with the potential temperature field. As a result, heat tags encode local generation information and remote connections involving material transport. The method is global rather than local, Eulerian rather than parcel-based, and allows for the potential temperature to be completely decomposed into a sum of heat tags with associated mixing ratios that sum to unity. The heat tag equations are constructed to retain positive and finite values, and thus are suitable for the examination of heat content of extended climate simulations.

Several complementary methods exist that should be considered in the context of the goals of this study. Heat tagging can be most closely compared to the construction of tracer spatial source Green’s functions to study atmospheric transport

Fajber’s current affiliation: Department of Atmospheric Sciences, University of Washington, Seattle, Washington.

Corresponding author: Robert Fajber, rfajber@uw.edu

from surface sources (e.g., [Holzer 1999](#); [Orbe et al. 2013, 2015](#)), or from the tropopause ([Orbe et al. 2013](#); [Waugh and Hall 2002](#)). The Green's function method can also be used to analyze the time scale of the transport ([Waugh and Hall 2002](#); [Holzer and Hall 2008](#); [Orbe et al. 2016](#)). Such boundary propagator methods transport tracers, subject to boundary conditions, typically with linear sources or sinks (e.g., the idealized loss functions in [Orbe et al. 2016](#)). In work of direct relevance to this study, [Orbe et al. \(2015\)](#) analyze the location of last boundary layer contact of air parcels in the Arctic troposphere. Boundary propagator methods are useful for problems that involve transport from a specified boundary surface and conservative transport, excepting for a linear loss function, through the bulk of the domain. Since the spatial complexity of internal diabatic heating sources and sinks do not lend themselves easily to the simplified loss parameterizations typically employed in boundary-impulse-response-based studies, and because potential temperature reflects the admixture of air masses from a broad region of surface "sources," propagator methods would require the tracers and the age spectrum of the Green's functions to be stored, which poses a computational problem.

Heat tagging is inspired by previous tagged tracer methods, including water tagging ([Sodemann et al. 2009](#); [Singh et al. 2016](#); [Dyer et al. 2017](#)), tracers of last saturation ([Galewsky et al. 2005](#)), and tagging of carbon monoxide and ozone ([Wang et al. 2011](#); [Fisher et al. 2017](#)). It builds on these methods by allowing for sources and sinks that are not sign definite without linearizing any terms in the thermodynamic equation. These are necessary changes to be able to track potential temperature in the atmosphere. [Martínez-Alvarado and Plant \(2014\)](#) study diabatic airmass generation and transport in an extratropical cyclone with a system similar to the one presented here, but with positive tags for heat sources and negative tags for heat sinks. Although this is suitable for the multiple day weather simulations they consider, the [Martínez-Alvarado and Plant \(2014\)](#) tag system would not remain finite in a long-term climate simulation. Our method overcomes this limitation by splitting the heating and cooling tendencies and treating cooling as a sink acting proportionally to all heat tags present ([section 2](#)), with the trade-off of having to include a sink term that is nonlinear in the tags.

A final complementary approach to that presented here is to use Lagrangian tracking of parcels undergoing heating and cooling as they pass through atmospheric blocks (e.g., [Pfahl et al. 2015](#)) or other circulation features. This requires tracking of a given circulation feature and, typically, an offline tool to be developed that uses frequent snapshots. The four heat tags used here are integrated consistently with the numerical methods used with other tracers like water vapor or chemical constituents, and thus are relatively easy to add to an already developed general circulation model (GCM). Additionally, Lagrangian parcel tracking requires the specification of criteria to decide which parcels to track, the pathlength to track the parcel over, etc. The advantage of the Eulerian approach is that it integrates over all possible forward paths, so it is free from these additional algorithmic choices.

We use a relatively simple model to provide an initial demonstration in a setting relevant to climate science. In particular,

we use the idealized aquaplanet model first developed by [Frierson et al. \(2006\)](#), and later by [O'Gorman and Schneider \(2008\)](#) and [Vallis et al. \(2018\)](#). The numerical methods and physical parameterizations used by the model simplifies the implementation of the heat tags for reasons that will be detailed in [section 2](#).

The results of our analysis are discussed in [section 3](#). The distribution of diabatic heating and cooling and the connection to the idealized physical parameterizations used in the model are discussed in [section 3a](#). In [section 3b](#), we calculate the globally integrated tag fractions to compare the lifetime of moisture in the atmosphere with the heat tags created from the condensation of moisture. The distribution of the tags and the tag fractions in the atmosphere are considered in [section 3c](#), which demonstrates the role of long-range transport in maintaining the heat content of the atmosphere. Heat tagging is used to decompose the variability of the potential temperature into contributions from different diabatic heating sources in [section 3d](#). The results show that the majority of the variability in the troposphere can be connected to the variability in tropical, convectively heated, air masses, but that these air masses coexist with cooler extratropical air masses. This is complemented by an airmass analysis in [section 3e](#), which shows distinctive tropical and extratropical surface air masses. Finally, in [section 3f](#), we decompose the vertically integrated poleward heat transport using the heat tags, which, because the transport is dominated by latent-heat related tags, illustrates the important role of the hydrological cycle.

This study covers heat tagging methodology and highlights selected scientific insights provided by this initial exploration. Our hope is that this study will serve as the basis for future exploration using this new method. In [section 4](#), we discuss the implications and potential applications for future study.

2. Methods

a. Tracer tagging

For a hydrostatic atmosphere in pressure coordinates, the conservation equation for a tracer c is

$$\frac{\partial c}{\partial t} = -\nabla \cdot (\mathbf{v}c) + D_H(c) + \sum_{i=1}^{N_s} S_i, \quad (1)$$

where $\mathbf{v} = (u, v, \omega)$ is the nondivergent fluid pressure-coordinate velocity satisfying $\nabla \cdot \mathbf{v} = 0$ and $S_i = \{S_1, \dots, S_{N_s}\}$ represents a set of N_s source and sinks of c . The term $D_H(c)$ represents horizontal diffusive flux of c . This represents a linear operation on c ; in this work it is considered to reflect numerical constraints and is not a focus for physical analysis. *Tracer tagging* decomposes the tracer c into a system of N_s tags, $\{c_1, \dots, c_{N_s}\}$ satisfying conservation of total field c at each point in space and time by locally constraining the tendency to conserve the total $\partial c / \partial t$

$$\sum_i^{N_s} \frac{\partial c_i}{\partial t} = \frac{\partial c}{\partial t} \quad (2)$$

and by identifying a time t_0 for which $\sum_{i=1}^{N_s} c_i(t_0) = c$ at each spatial point.

We wish to constrain c_i to be positive semidefinite:

$$c_i \geq 0, \quad i = 1, \dots, N_S. \quad (3)$$

This constraint will be violated by the simple decomposition of (1)

$$\frac{\partial c_i}{\partial t} = -\nabla \cdot (\mathbf{v}c_i) + D_H(c_i) + S_i, \quad i = 1, \dots, N_S \quad (4)$$

in which each tag c_i has a corresponding source or sink S_i , and for which sink processes will tend to generate negative c_i while conserving the total $c = \sum_{i=1}^{N_S} c_i$. [Martínez-Alvarado and Plant \(2014\)](#) used such a system to track sources and sinks of potential temperature in short-term weather forecasts. In the context of climate analysis, however, such a system leads to nonstationary behavior in the tags. For example, if $S = S_0 + S_1$ where S_0 is positive everywhere and S_1 is negative everywhere [e.g., if c represents potential temperature, S_0 could represent latent heating and S_1 longwave cooling, analogously to [Martínez-Alvarado and Plant \(2014\)](#)], c_0 and c_1 would diverge to positive and negative infinite values even while conserving the total c .

To guarantee (3), we first decompose S_i at each spatial and temporal point into positive sources and negative sinks:

$$S_i = S_i^+ + S_i^-, \quad (5)$$

where

$$S_i^+ = I(S_i)S_i \quad (6)$$

and

$$S_i^- = I(-S_i)S_i, \quad (7)$$

for $i = 1, \dots, N_S$. In (6) and (7), I is the Heaviside function, which is 1 for a positive argument and 0 otherwise. Thus, S_i^+ represents the positive source of S_i and S_i^- represents the negative sink of S_i .

If we wish to track different sources of c in the atmosphere, then it makes sense to have each tag c_i correspond to each S_i^+ , which we will use as a source for that tag. To create the sink for the tag we will assume that the tags in any given air parcel are well mixed, and that the total tracer sink,

$$S^- = \sum_{i=1}^{N_S} S_i^-, \quad (8)$$

does not act to preferentially remove any given tracer tag. Under these assumptions, the sink term for c_i can be written as

$$S_i^- := \frac{c_i}{c} S^- = \chi_i S^-, \quad \text{where } \chi_i := \frac{c_i}{c} \quad (9)$$

is a *tag fraction* for tag i . In other words, the sink removes different tags proportionally to their amount inside the parcel. Putting together these considerations gives the system of tracer tags

$$\frac{\partial c_i}{\partial t} = -\nabla \cdot (\mathbf{v}c_i) + D_H(c_i) + S_i^+ + \chi_i S^-, \quad i = 1, \dots, N_S, \quad (10)$$

where the S_i^+ are defined by (5) and (6) and where we have used (9). The c_i are initialized at t_0 to have a positive value and satisfy

$$c(t_0) = \sum_{i=1}^{N_S} c_i(t_0). \quad (11)$$

It is easily shown that (10) guarantees that tag tendencies $\partial c_i/\partial t$ sum to the total tendency, $\partial c/\partial t$, so (2) is satisfied.

The tag fractions $\{\chi_i\}$ defined in (9) sum to unity

$$\sum_{i=1}^{N_S} \chi_i = 1. \quad (12)$$

Their evolution equations can be obtained by first recognizing that

$$\frac{\partial(\cdot)}{\partial t} + \nabla \cdot (\mathbf{v}\cdot) + D_H(\cdot)$$

is a linear differential operator on its argument (for non-divergent pressure-coordinate \mathbf{v}). Taking $c^{-1} \times$ (10) and subtracting $\chi_i c^{-1} \times$ (1) then yields

$$\frac{\partial \chi_i}{\partial t} = -\nabla \cdot (\mathbf{v}\chi_i) + D_H(\chi_i) + (1 - \chi_i) \frac{S_i^+}{c} - \chi_i \sum_{j \neq i} \frac{S_j^+}{c}. \quad (13)$$

Note that the sink terms S_i^- do not explicitly appear in this equation, which demonstrates the tradeoffs between the relative fraction of the tags: although S_i^- do not decrease χ_i , sources of other tags, $(\{S_j^+\}_{j \neq i})$, will act to decrease χ_i to guarantee (12). This observation will prove useful in understanding the distribution of heat tag fractions in [section 3](#).

Equation (13) demonstrates that if the tracer field c is positive, the tag fractions c_i are also positive because $(1 - \chi_i)(S_i^+/c)$ will not increase χ_i above 1, and $-\chi_i \sum_{j \neq i} (S_j^+/c)$ will not decrease χ_i below 0, so $0 \leq \chi_i \leq 1$. Since $c_i = \chi_i c$, then $0 \leq c_i \leq c$.

Since the $\{c_i\}$ are positive and, via (2) and (11), sum to c for all time, they remain bounded by the greatest value of c . This ensures that the system will not diverge even under long time integration, making this formulation useful for equilibrium climate integrations.

Last, we comment on initializing the system. Perhaps the most generic way to initialize the system is to introduce an ‘‘initialization tag’’ c_{N_S+1} , which evolves according to

$$\frac{\partial c_{N_S+1}}{\partial t} = -\nabla \cdot (\mathbf{v}c_{N_S+1}) + D_H(c_{N_S+1}) + \chi_{N_S+1} S^-,$$

[with all of the other tags evolving normally according to Eq. (10)], and then set $c_{N_S+1}(t_0) = c(t_0)$, and set all the other tags to 0. The new system of tags still satisfies (2); however, the initialization tag will decay toward 0 while the other tags approach their equilibrium values, and the concentration of c_{N_S+1} measures how much of the initial tracer field has not decayed. This is essentially what is done for the initial water vapor field in weather applications ([Sodemann et al. 2009](#)).

While using an initialization tag gives some additional information, the decay time scale can be very long for some cases. In this case, it is advantageous to set the tag which takes the longest time to be produced to be $c(t_0)$, and the other tags to be 0. This can significantly reduce the amount of time for the model to spin up to an equilibrium time. The specifics of the initialization for heat tags is discussed at the end of this section, where we utilize this second approach to reduce the amount of spinup time needed.

b. A conceptual example

A conceptual example motivates this method: consider transport, generation, and loss in one (meridional) dimension for a tracer $c = c_1 + c_2$ partitioned into two tags with source/sink terms $S = S_1 + S_2$:

$$\frac{\partial c}{\partial t} + \frac{\partial(vc)}{\partial y} = S,$$

$$\frac{\partial c_i}{\partial t} + \frac{\partial(vc_i)}{\partial y} = S_i^+ + \chi_i S_i^-, \quad \text{where } \chi_i = \frac{c_i}{c}, i = 1, 2.$$

Mass and tracer conservation require $\langle v \rangle = 0$ and $\langle S \rangle = 0$, where $\langle \cdot \rangle$ indicates the time and meridional mean over the domain $y \in [0, L]$.

Assuming the tags are well mixed (and thus that covariance between c_1 , c_2 , and v are unimportant), we can estimate

$$\langle \chi_i \rangle \approx \langle \chi_i \rangle^{\text{mixed}} = \langle S_i^+ \rangle / \langle S^- \rangle$$

(see section 3a). However, to obtain more information about how each tag contributes locally to the structure of c requires explicit calculation.

As an example of such a calculation, we restrict the sources of c , S_i^+ , to only be allowed to have positive values in the equatorial half of the domain $y \in [0, L/2]$. Thus, tags can only be produced in this region, whereas they can be transported and destroyed over the whole domain. Now consider a situation in which S_1 is sourced only for poleward flow and S_2 is sourced only for equatorward flow. That is, $S_1^+ > 0$ for $v > 0$ and $S_2^+ > 0$ for $v < 0$, again for $y \in [0, L/2]$. Then c in the polar half of the domain would consist solely of c_1 , i.e., $\chi_1 = 1$, $\chi_2 = 0$ for $y \in [L/2, L]$, and the entire poleward flux of c at $y = L/2$ would be from c_1 . Although this example seems somewhat contrived, the fictional c_1 is not that far from the convective tag, as shown in section 3.

From this example it can be seen that the tags provide a way to attribute the tracer distribution to processes far from the source regions. In our simplified system it might seem that the tags are not necessary; however, this is because the circulation is greatly simplified. For more realistic three-dimensional circulations the mass transport can be highly complicated, and so the connection between tracer content in remote regions and their sources is difficult to determine without the tracer tags.

c. Numerical implementation in an idealized moist general circulation model

We use the implementation of the class of idealized moist general circulation model developed in Frierson et al. (2006), Frierson (2007), and O’Gorman and Schneider (2008) that is found in the Isca framework (Vallis et al. 2018). This model, coded with the NOAA GFDL Flexible Modeling System, solves the moist hydrostatic primitive equations on the sphere using a pseudospectral method. The Isca framework provides a set of standard physical parameterizations, including updated radiative transfer schemes. The horizontal resolution of the spectral core is T85 and in the vertical there are 30 levels evenly spaced in the model’s sigma coordinate. A fourth-order

hyperviscosity with a base coefficient of 0.1 day^{-1} that is applied to the highest resolved wavenumber is used. The atmosphere is situated above a global slab ocean with a depth of 100 m. The model is run with annual average insolation and without a diurnal cycle. The boundary conditions and boundary forcing are zonally homogeneous and hemispherically symmetric about the equator. The long-term statistics are expected to respect these related symmetries such as hemispheric symmetry and no stationary waves.

Potential temperature and tracers, including water vapor, are advected using the model’s standard spectral advection scheme. For water vapor solely, a hole-filling scheme is used to preserve nonnegativity. Although a spectral advection scheme does not guarantee nonnegativity (Rasch and Williamson 1990), negative values were mitigated by reducing the time step of the model to 150 s for both the dynamics and physical parameterizations.

Of the various combinations of sub-grid-scale physical parameterizations and radiative transfer available within the Isca framework, we select the following:

- 1) A two-stream, two-plus-one band, gray radiation scheme, described in section 4.2 of Vallis et al. (2018). The scheme parameterizes the optical depth in terms of a nominal CO_2 concentration value and of the water vapor field in the model. It includes a shortwave window, a longwave band that treats the infrared window region of the spectrum, and another longwave band that treats the rest of the spectrum. The radiative scheme used in our version of the model has a nominal CO_2 value of 360 ppm [documented in section 4.2 in Vallis et al. (2018)]. In section 4.6, this value is doubled to explore the response to climate change.
- 2) A vertical diffusion that parameterizes turbulent boundary layer fluxes using simplified Monin–Obukhov similarity theory (Frierson et al. 2006). The effect of this parameterization is to spread the surface fluxes of enthalpy, moisture, and momentum over the model planetary boundary layer. The surface fluxes appear in the atmospheric tendencies through this parameterization.
- 3) A large-scale condensation scheme that removes water vapor and adds latent heat to a grid cell if the grid cell reaches saturation. The water vapor is assumed to be immediately removed from the atmosphere without allowing for reevaporation. This is different from Frierson et al. (2006), but is the same formulation that was used in O’Gorman and Schneider (2008).
- 4) A subgrid-scale convection scheme that is the “shallower” option documented in Frierson (2007). The convection scheme checks if there is convective available potential energy in a column and, if there is, relaxes the column toward a moist adiabatic profile in a manner that conserves total column enthalpy.

The tracer tagged here is potential temperature θ , which evolves according to

$$\frac{\partial \theta}{\partial t} = -\nabla \cdot (v\theta) + D_H(\theta) + \Pi Q, \quad (14)$$

where the Exner function $\Pi = (p_0/p)^\kappa$ and Q represents the sum of the model’s parameterized heating rates. The development of the

TABLE 1. Tagged tracer symbols for the generic tracer introduced in section 2a and for the heat tags introduced in section 2c.

Variable name	Generic symbol	Heat tag specific symbol	Defining equations
Total tracer	c	θ	(1), (14)
Tag from process i	c_i	θ_i	(4), (19a)–(19d)
Tag fraction from process i	$\chi_i = c_i/c$	$\chi_i = \theta_i/\theta$	(20), (21)
Nonconservative tendency i	S_i	ΠQ_i	(5), (16)
Tag source for process i	S_i^+	ΠQ_i^+	(6), (17)
Total cooling	S^-	ΠQ^-	(7), (18)
Tag sink for process i	$\chi_i S^-$	$\chi_i \Pi Q^-$	(9), (19a)–(19d)

heat tags follows by applying the generic tracer tagging methods in section 2a to Eq. (14). Table 1 summarizes this correspondence, and the rest of the section develops the idea in full.

We use Eq. (10) as follows: we identify θ with c , set $N_S = 4$ tags, and following the correspondence in Table 1,

$$\theta = \sum_{i=1}^{N_S} \theta_i = \theta_{\text{conv}} + \theta_{\text{cond}} + \theta_{\text{diff}} + \theta_{\text{radi}}, \quad (15)$$

and split the heating terms into θ sources and sinks,

$$\Pi Q = \Pi Q^+ + \Pi Q^-, \quad (16)$$

with

$$\Pi Q^+ = \Pi Q_{\text{conv}}^+ + \Pi Q_{\text{cond}}^+ + \Pi Q_{\text{diff}}^+ + \Pi Q_{\text{radi}}^+ \quad (17)$$

and

$$\Pi Q^- = \Pi Q_{\text{conv}}^- + \Pi Q_{\text{diff}}^- + \Pi Q_{\text{radi}}^-. \quad (18)$$

Here, the subscripts conv, cond, diff, radi indicate, respectively, heating from the subgrid-scale convection scheme, the large-scale condensation, the vertical diffusion in the boundary layer parameterization, and the shortwave and longwave radiative transfer schemes. This is summarized in Table 2. Note the absence of Q_{cond}^- in (18). This is zero by design, because the model precipitation scheme has no reevaporation of falling water vapor (cooling and hence a θ sink). Applying Eq. (10) to θ yields a set of tracers that evolve according to

$$\frac{\partial \theta_{\text{conv}}}{\partial t} = -\nabla \cdot (\mathbf{v} \theta_{\text{conv}}) + D_H(\theta_{\text{conv}}) + \Pi \left(Q_{\text{conv}}^+ + \frac{\theta_{\text{conv}}}{\theta} Q^- \right), \quad (19a)$$

$$\frac{\partial \theta_{\text{cond}}}{\partial t} = -\nabla \cdot (\mathbf{v} \theta_{\text{cond}}) + D_H(\theta_{\text{cond}}) + \Pi \left(Q_{\text{cond}}^+ + \frac{\theta_{\text{cond}}}{\theta} Q^- \right), \quad (19b)$$

$$\frac{\partial \theta_{\text{diff}}}{\partial t} = -\nabla \cdot (\mathbf{v} \theta_{\text{diff}}) + D_H(\theta_{\text{diff}}) + \Pi \left(Q_{\text{diff}}^+ + \frac{\theta_{\text{diff}}}{\theta} Q^- \right), \quad (19c)$$

$$\frac{\partial \theta_{\text{radi}}}{\partial t} = -\nabla \cdot (\mathbf{v} \theta_{\text{radi}}) + D_H(\theta_{\text{radi}}) + \Pi \left(Q_{\text{radi}}^+ + \frac{\theta_{\text{radi}}}{\theta} Q^- \right). \quad (19d)$$

The sources and sinks are separated at every grid point and time step in the model. For instance, in a convectively unstable column the convection scheme heats higher model levels,

contributing locally to Q_{conv}^+ , and cools lower model levels, contributing locally to Q_{conv}^- and hence to Q^- [in Eqs. (18) and (19a)]. Apart from small numerical errors discussed in the next subsection, the tag sum should satisfy (15) at every time step and grid point.

For heat tag fractions

$$\chi_i = \frac{\theta_i}{\theta}, \quad i = 1, \dots, 4, \quad (20)$$

the corresponding evolution [see Eq. (13)] is

$$\frac{\partial \chi_i}{\partial t} = -\nabla \cdot (\mathbf{v} \chi_i) + D_H(\chi_i) + (1 - \chi_i) \frac{\Pi Q_i^+}{\theta} - \chi_i \sum_{j \neq i} \frac{\Pi Q_j^+}{\theta}. \quad (21)$$

The model tagging procedure generates physical tendencies at every time step, separates them into their positive and negative parts, generates the tracer tendencies above, and then passes these to the tracer advection scheme. This numerical procedure is simplified for the idealized moist model, since it only has a single time step for both the physics and dynamics.

Initialization and equilibration of the tag tracers are represented in Fig. 1. Experimentation (not shown) reveals that the radiative tag radi, which we will find to be sourced and largely confined to the stratosphere (section 3), takes several years to equilibrate, which is an order of magnitude longer than found for the other tags, owing to the relatively long lifetime of stratospheric air masses (Hall and Plumb, 1994). In the experiments reported here, the heat tag is initialized by setting θ_{radi} to θ and all other tags to zero, which satisfies total tag conservation (15) by construction, and which is designed to bring the full set more quickly into equilibrium. Figure 1 shows the time evolution of the globally averaged tracer tag fractions $\{\chi_i\}$, which reveals the relatively fast equilibration of χ_{conv} , χ_{cond} , and χ_{diff} compared with χ_{radi} .

After approximate statistical equilibrium is reached (e.g., after day 2000 for the simulation in Fig. 1), the following 2500 days of simulation is used as an analysis period. We denote by an overbar the zonal mean and time mean (for this

TABLE 2. Heat tag names used throughout the paper.

No.	Long name	Symbol
1	Convection tag	θ_{conv}
2	Condensation tag	θ_{cond}
3	Diffusion tag	θ_{diff}
4	Radiation tag	θ_{radi}

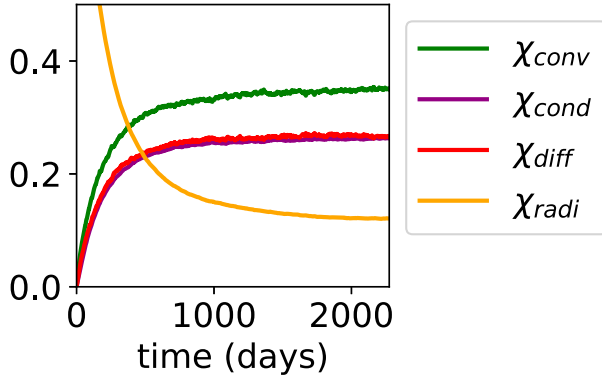


FIG. 1. Time evolution of the globally averaged tracer tag fractions χ_i during the tag spinup.

analysis period). The error associated with total tag conservation is measured by

$$R = \left[\frac{1}{T} \int_0^T (1 - \sum_i \chi_i)^2 dt \right]^{1/2}. \quad (22)$$

The error is less than 1% throughout most of the troposphere, and less than 2% everywhere below 200 hPa (Fig. 2).

3. Results

a. Distribution of tracer sources and sinks

The climatological distribution of tag sources for θ_i , $\{\Pi Q_i^+\}$, is shown in Figs. 3a–d and the climatological distribution of tag sinks for θ_i , $\{\Pi Q_i^-\}$, is shown in Figs. 3e–h. The distribution of convection and condensation sources (ΠQ_{conv}^+ and ΠQ_{cond}^+ , Figs. 3a,b) shows the partitioning between large-scale and subgrid-scale latent heating. In the tropical midtroposphere, most of the latent heating happens through the subgrid-scale convective parameterization. There is a strong isolated maximum in condensation source in the tropical upper troposphere that is approximately half the maximum of the convection source. This reflects saturation of air that is explicitly resolved by the model, which occurs at the top of the Hadley cell's region of strong vertical ascent. A small amount of shallow convection heat tag source also extends into the subtropics and midlatitudes. In the midlatitudes, condensation becomes the dominant tag source of latent heating (Fig. 3b). In this region, regions of vertical ascent associated with baroclinic eddies create conditions for large-scale saturation. Cooling in the convective parameterization (ΠQ_{conv}^-) only occurs weakly in a location near the tropical surface (Fig. 3e), reflecting the rare occasions when the convective parameterization acts to cool the lower troposphere. By definition, ($\Pi Q_{\text{cond}}^- \equiv 0$). Overall, latent heating is the greatest source of heating in the model, and plays a very minor role in cooling.

The diffusive heat tag source, ΠQ_{diff}^+ (Fig. 3c), is greatest near the surface, and its distribution reflects the height of the planetary boundary layer in the model atmosphere (Frierson et al. 2006). There is also strong diffusive heating near the tropical surface, where the hot surface provides large sensible

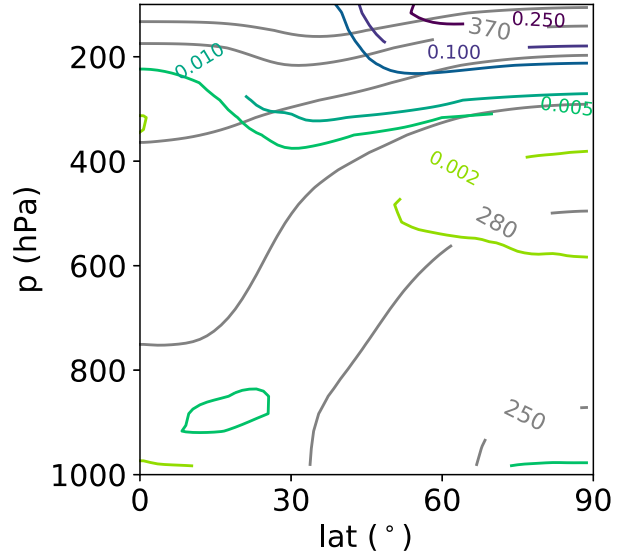


FIG. 2. The root-mean-squared residual between θ and the sum of the tagged tracers, given by Eq. (22). The gray lines show $\bar{\theta}$ with a contour interval of 30 K.

heat fluxes into the atmosphere. There is cooling present throughout the lower and midtroposphere from the diffusive parameterization (ΠQ_{diff}^- , Fig. 3g). This cooling is due to boundary layer mixing that occurs when the boundary layer extends relatively deeper into the troposphere. This pattern of diffusive heating below the boundary layer and diffusive cooling above the boundary layer is also seen in the storm tracks (Ling and Zhang, 2013).

Radiative heating is the only tag source term in the stratosphere, visible in these plots only toward the equator. This heating reflects the parameterized shortwave absorption by ozone. As expected, the cooling from the radiative scheme (Fig. 3h) extends throughout the atmosphere. The greatest cooling rates are in the tropical upper troposphere, where the thin optical depth above allows for the upwelling radiation to leave the atmosphere.

b. Globally integrated tag fractions

We denote by angle brackets the climatological global mean, and by an asterisk the deviation from the global mean. The evolution equation for the heat tags [Eq. (14)], globally and time averaged, yields

$$\langle \chi_i \rangle = \frac{\langle \Pi Q_i^+ \rangle}{|\langle \Pi Q^- \rangle|} + \frac{\langle (\chi_i)^* (\Pi Q^-)^* \rangle}{|\langle \Pi Q^- \rangle|}. \quad (23)$$

The term $\langle (\chi_i)^* (\Pi Q^-)^* \rangle$ represents the effect of the spatial distribution of θ_i on the global mean of $\langle \chi_i \rangle$. If the atmosphere were well mixed, then $\chi_i^* = 0$, so we can define a well-mixed estimate

$$\langle \chi_i^{\text{mixed}} \rangle = \frac{\langle \Pi Q_i^+ \rangle}{|\langle \Pi Q^- \rangle|}, \quad (24)$$

which is the value the tag would have if it were well mixed.

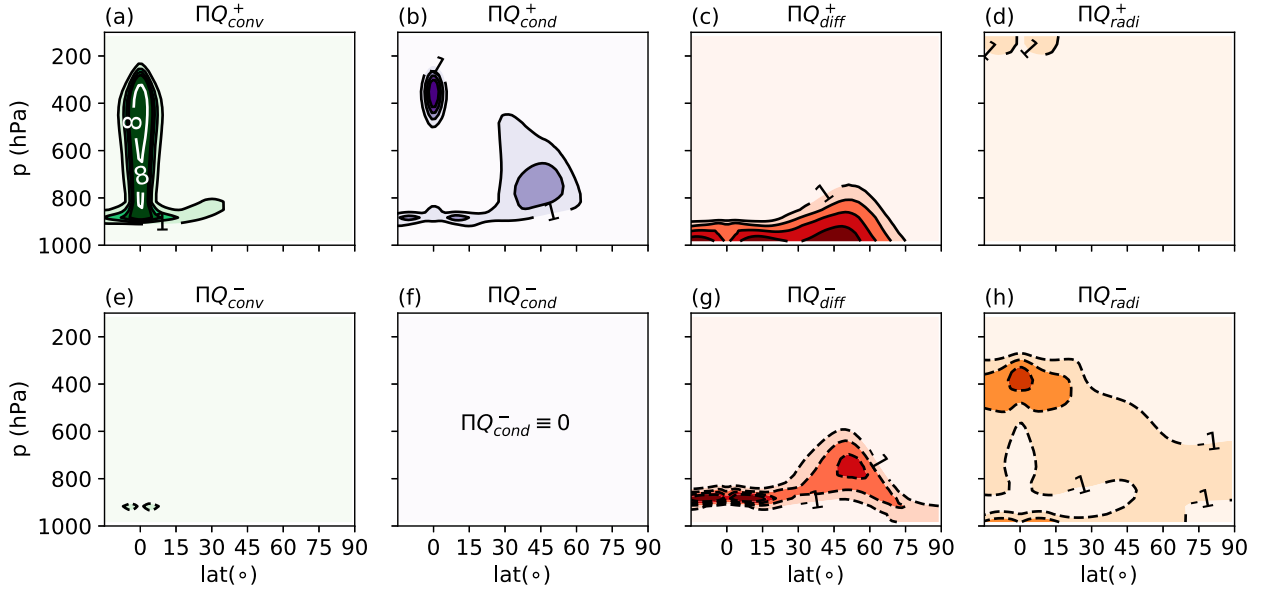


FIG. 3. (a) Zonal mean climatological positive θ tendency from Q_{conv} (contour interval: 1 K day^{-1}). (b)–(d) As in (a), but for Q_{cond} , Q_{diff} , and Q_{radi} . (e)–(h) As in (a)–(d), but for the negative θ tendency. Extra contours are marked in white.

The well-mixed values for the four heat tags, shown in Table 3, suggests that in this model just under one-third of the θ content of the atmosphere should be generated by each of subgrid-scale convection, large-scale convection, and vertical diffusion. The remaining small fraction of heat tag arises from shortwave radiation in the stratosphere. The differences between the well-mixed estimates and the actual values reflect the extent to which tags are prevented from being well mixed (visible in Fig. 4). The well-mixed estimate of $\langle \chi_{conv} \rangle$, $\langle \chi_{cond} \rangle$, and $\langle \chi_{diff} \rangle$ are within 20% of their actual values, suggesting that these heat tags, especially the convective tag, are indeed rapidly mixed throughout the atmosphere. The $\langle \chi_{cond} \rangle$ and $\langle \chi_{conv} \rangle$ are somewhat lower than their well-mixed estimates, suggesting that diabatic cooling acts more efficiently on these tracers, i.e., $\langle (\chi_i)^* (\Pi Q^-)^* \rangle < 0$. The radiative tag fraction is a factor of 4 greater than its well-mixed estimate, suggesting strong isolation and relatively little loss from radiation, i.e., $\langle (\chi_i)^* (\Pi Q^-)^* \rangle > 0$.

The contribution of each heat tag to total atmospheric heat content (both moist and dry contributions to the moist static energy) is quantified through partitioning of equivalent potential temperature θ_e :

$$1 = \left\langle \frac{\theta_e}{\theta_e} \right\rangle \approx \sum_{i=1}^4 \left\langle \frac{\theta_i}{\theta_e} \right\rangle + \left\langle \frac{L_v q}{C_p \theta_e} \right\rangle, \quad (25)$$

where q is specific humidity (see the third column of Table 3), and we have used the approximate relationship (similar to Shaw and Pauluis 2012), $\theta_e \approx \theta + L_v q / C_p$.

Table 1 shows that the heat tags associated with latent heating (conv and cond) contribute almost 40 times as much heat content as the direct contribution of moisture ($L_v q / C_p$). This can be viewed as a consequence of the relatively rapid cycling of water vapor in the hydrological cycle compared

to the relatively slow cycling of heat content. This assertion is supported by, first, approximating the time mean budget for $\langle q \rangle$ as

$$0 \approx \langle E \rangle - \frac{\langle q \rangle}{\tau_q},$$

where E is the evaporation, and precipitation has been represented by a relaxation to 0 with lifetime τ_q ; and second, by approximating the budget for the heat content associated with latent heating by

$$0 \approx \left\langle \frac{L_v C}{c_p} \right\rangle - \frac{\langle \theta_C \rangle}{\tau_C},$$

where C is the condensation (including subgrid-scale and resolved condensation, so that $\theta_C = \theta_{conv} + \theta_{cond}$), and cooling has been represented as a relaxation to 0 with time scale τ_C . Noting that $\langle E \rangle \approx -\langle C \rangle$,

$$\frac{\langle L_v q / c_p \rangle}{\langle \theta_C \rangle} \approx \frac{\tau_q}{\tau_C}. \quad (26)$$

TABLE 3. Well-mixed estimate, globally averaged tag fractions with respect to θ , $\langle \chi_i \rangle$, and the globally averaged tag fractions with respect to θ_e , $\langle \theta_i / \theta_e \rangle$.

i	Heat tag/tracer	$\langle \chi_i^{mixed} \rangle$	$\langle \chi_i \rangle$	$\left\langle \frac{\theta_i}{\theta_e} \right\rangle$
1	conv	0.337	0.325	0.320
2	cond	0.299	0.264	0.259
3	diff	0.299	0.274	0.269
4	radi	0.051	0.139	0.139
—	$\frac{L_v}{C_p} q$	—	—	0.015

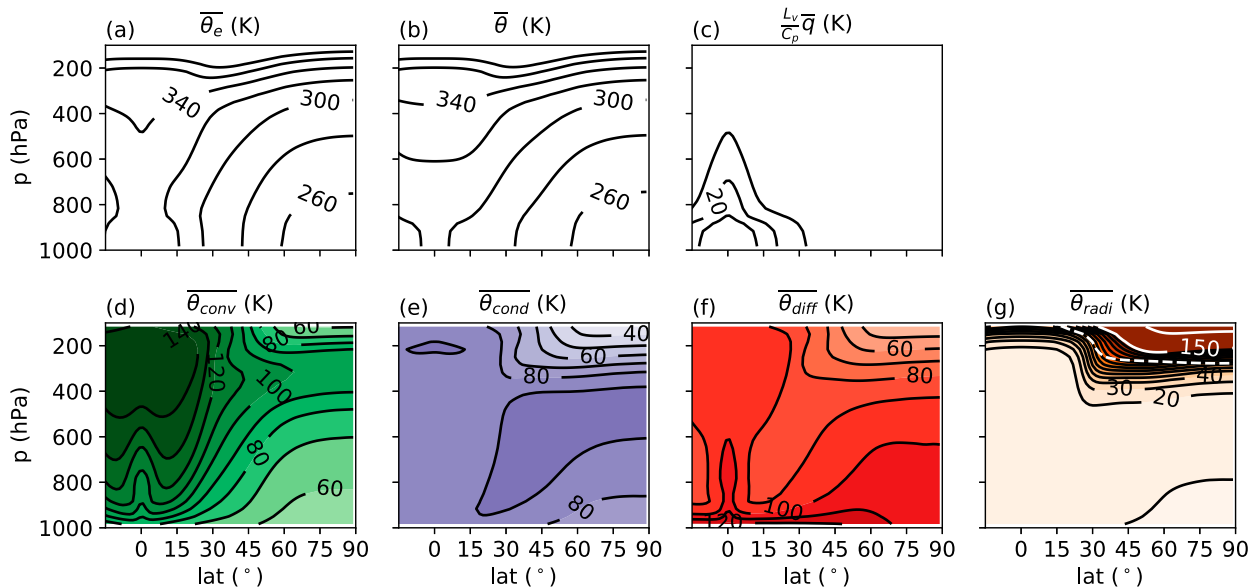


FIG. 4. (a) Zonal mean climatological equivalent potential temperature θ_e (contour interval: 20 K). (b) As in (a), but for the potential temperature θ . (c) As in (a), but for the humidity normalized to temperature units $(L_v/C_p)q$ (contour interval: 10 K). (d) Zonal mean climatologies of θ_{conv} (contour interval: 20 K). (e)–(g) As in (a), but for θ_{cond} , θ_{diff} , and θ_{radi} . The dashed white line in (g) is the estimate of the dynamical tropopause, defined as the 1.5 potential vorticity unit surface calculated using climatological mean quantities. Extra contours are marked in white.

The partitioning of heat content in the third column of Table 3 can be interpreted as reflecting the long lifetime of the heat tags related to latent heating (dissipated by radiative cooling to space over several weeks) compared to the short lifetime of water vapor (which is rapidly removed by precipitation over a few days). This ratio may be model dependent, and could change with different model parameterizations or climatological regimes.

c. Zonal mean tag distribution

We begin the discussion of the global distribution of tags by showing the climatological distribution of $\bar{\theta}_e$ (Fig. 4a) and its decomposition into dry and moist components using $\bar{\theta}_e \approx \theta + (L_v/C_p)q$ (Figs. 4b,c). The moist stratification is unstable in the tropics, near neutral in the midlatitudes, and stable at the poles. The moisture content in the atmosphere is primarily confined to the tropical surface, which explains the unstable stratification in the tropics. The potential temperature can be further subdivided using the heat tags, so that Fig. 4b is the sum of Figs. 4d–g.

The climatological distribution of the heat tags is shown in Figs. 4d–g. The distribution of the heat tags reflects their creation and loss by diabatic heating and cooling (Fig. 3) as well as atmospheric transport. For instance, θ_{diff} is produced only below about 700 hPa, but because there is insufficient cooling near the surface to balance the tag source, θ_{diff} is distributed through a larger region of the atmosphere.

The convective heat tag θ_{conv} (Fig. 4d) has a maximum in the deep tropics where the greatest source is located (Fig. 3a). The large transfer of energy from the surface to the atmosphere in the deep tropics generates convection, which creates large

amounts of θ_{conv} , and drives the Hadley circulation, which transports θ_{conv} from the lower troposphere to the upper troposphere. These effects combined create a large amount of θ_{conv} in the deep tropics with a strong vertical gradient from the surface to the upper troposphere. Thus, the tropical upper-tropospheric gradient of $\bar{\theta}$ (Fig. 4b) is attributable to this convective process. Between 15° and 30° the vertical gradient is considerably reduced. This region is in the downwelling branch of the Hadley cell, which transports θ_{conv} from the upper troposphere to the lower troposphere.

Outside the tropics, θ_{conv} has a large meridional extent, with values as high as 60–90 K over the poles. In the extratropics $\bar{\theta}_{conv}$ is greatest in the upper troposphere.

The condensation tracer tag θ_{cond} has a maximum in the midlatitudes, near 45°. Since this is a region of descent in the climatological zonal mean, the vertical uplift required to bring the parcels to saturation comes from regions of ascent inside midlatitude eddies (Schemm et al. 2013; Pfahl et al. 2015). The maximum of $\bar{\theta}_{cond}$ is above and poleward of the midlatitude maximum of ΠQ_{cond}^+ , indicative of the transport away from the source. Thus the baroclinic eddies act not just to generate latent heating in the midlatitudes, but also to transport θ_{cond} away from its source region.

The diffusive heat tag $\bar{\theta}_{diff}$ is greatest near the surface. The strong vertical near-surface gradient in the tropics and midlatitudes reflects the near-surface diffusive heat source and the diffusive cooling sink immediately above. In the tropics, there is an intrusion of high- θ_{diff} air that extends into the midtroposphere and that compensates for the reduced contribution of θ_{conv} in this region. This leads to weak meridional gradients of θ in this region (Fig. 4b), and suggests a dynamical

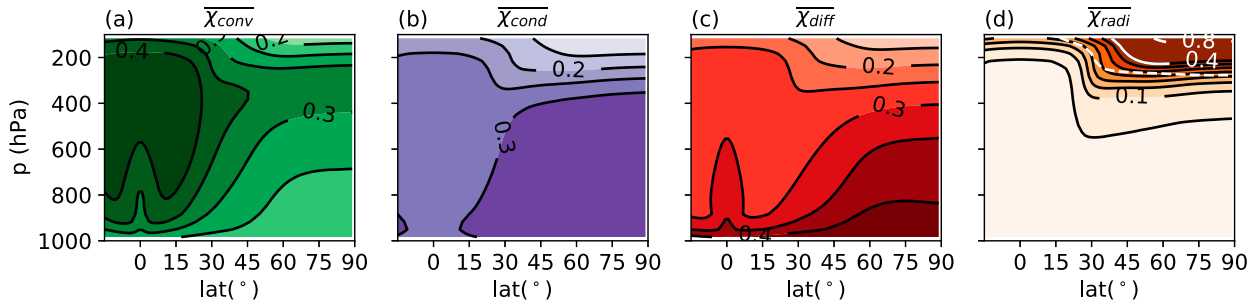


FIG. 5. (a)–(d) As in Figs. 4d–g, but for the corresponding tag fractions χ_i (contour interval: 0.05). Extra contours are marked in white.

compensation between diffusive and convective processes in the deep tropics that will be further discussed below. In the midlatitudes, there is a strong vertical gradient over the regions where Q_{diff}^+ is nonzero. Poleward of this, the vertical gradient is reduced, suggesting vertical mixing of θ_{diff} as air masses are advected poleward. There is a tongue of relatively low- θ_{diff} air extending from the midlatitude upper troposphere into the subtropics, suggesting that this air mass has not recently been in contact with the surface. This is similar to the results of (Galewsky et al. 2005), who show that the air mass in the subtropics primarily comes from the isentropic descent from the upper troposphere.

Because there is little shortwave heating in the troposphere, θ_{radi} is primarily found in the stratosphere and dominates the other heat tags there. The strong gradients of θ_{radi} effectively trace out the dynamical tropopause in the extratropics (dashed white line in Fig. 4g). In this model, stratospheric air intrusions into the troposphere are too infrequent and/or weak to maintain large values of θ_{radi} in the presence of radiative cooling (θ_{radi} sink) in the troposphere.

The spatial distribution of the tag fractions (Figs. 5a–d) give complementary information to the zonal means of the heat tags. While the θ_i express a balance between the sources Q_i^+ and sinks Q^- [Eqs. (19a)–(19d)], the χ_i express tradeoffs between the different sources Q_i^+ [Eq. (13)]. We thus expect χ_i to be largest in regions where Q_i^+ is large compared to the other $Q_{j \neq i}^+$. Thus $\overline{\chi_{conv}}$ is dominant in the upper troposphere where there is strong convective heating and $\overline{\chi_{radi}}$ (Fig. 4h) is reduced in the troposphere where other tag sources dominate.

The convective tag fraction $\overline{\chi_{conv}}$ (Fig. 5a) peaks in the tropics and accounts for just under half the total θ content in that region. The χ_{conv} tag fraction extends into the polar upper troposphere, where it remains as much as 30% of the total, consistent with its well-mixed estimate. This complements the analysis of Orbe et al. (2015), who show that a large amount of tropical air mass sourced at the tropical surface and undergoing conservative advection is then transported to the tropical upper troposphere and then to the Arctic upper troposphere. Similarly χ_{conv} , which is sourced in the tropics, extends throughout the upper troposphere, which demonstrates a transport pathway between the tropical and polar upper troposphere. Additionally, for the heat tags as formulated here, the identity of convective tag is robust even in the presence of diabatic cooling from radiation.

The condensation tag fraction $\overline{\chi_{cond}}$ is greatest in the extratropics, and accounts for about 30% of the θ content of

midlatitude free troposphere and polar tropospheric air (Fig. 5b), which is, again, consistent with its well-mixed estimate. The maximum θ_{cond} in the Arctic is located in the midtroposphere, below the upper-tropospheric maximum of Arctic θ_{conv} . These characteristics resemble air sourced at the midlatitude surface and undergoing conservative advection (Orbe et al. 2015). The large contribution to θ in the polar column could also be anticipated from Fajber et al. (2018), who showed that the poleward transport of warm air was associated with latent heating in the midlatitudes. It should be noted that $\overline{\chi_{cond}} + \overline{\chi_{conv}}$ amounts to more than 60% throughout most of the polar troposphere, despite the lack of latent heating in the polar atmosphere.

The diffusive tag makes up at least 40% of the potential temperature in the boundary layer, and this fraction increases from the equator to the pole (Fig. 5c). This follows the change in the ratio of the surface sensible to surface moisture fluxes, which also increases from the equator to the pole. As the boundary layer air gets colder it also becomes drier at a faster rate. This increases the fraction of the diffusive tracer tag near the polar and midlatitude boundary layer. Low amounts of χ_{diff} are seen in the subtropical upper troposphere. This is similar to the results of Galewsky et al. (2005), who show that air in the subtropics is transported there from the upper troposphere, where the air mass has relatively little θ_{diff} .

The distribution of $\overline{\chi_{radi}}$ (Fig. 5d) is similar to the distribution of θ_{radi} . Since the tropospheric radiative heating is small compared with the other sources of tropospheric heating, $\overline{\chi_{radi}}$ is small compared to the other tag fractions there.

d. Dynamic variability of the heat tags

The distributions of the individual heat tags $\{\theta_i\}$ (Figs. 4d–g) feature more spatial structure than their sum ($\bar{\theta}$, Fig. 4b), suggesting that the distributions are not independent. Such relationships are also evident in snapshots like Fig. 6, which shows, at a typical time in the simulation, the vertical mean of χ'_{conv} , χ'_{cond} , χ'_{diff} , and χ'_{radi} , where the prime indicate the deviation from the time and zonal mean. In the tropics and midlatitudes, there are regions with coincident opposite-signed anomalies of χ_{cond} and χ_{conv} . Anomalies of χ_{cond} and χ_{radi} are relatively weak in the tropics and strong in the extratropics, and also feature coincident opposite signed anomalies.

Thus motivated to further explore these relationships, we analyze a decomposition of the potential temperature variance:

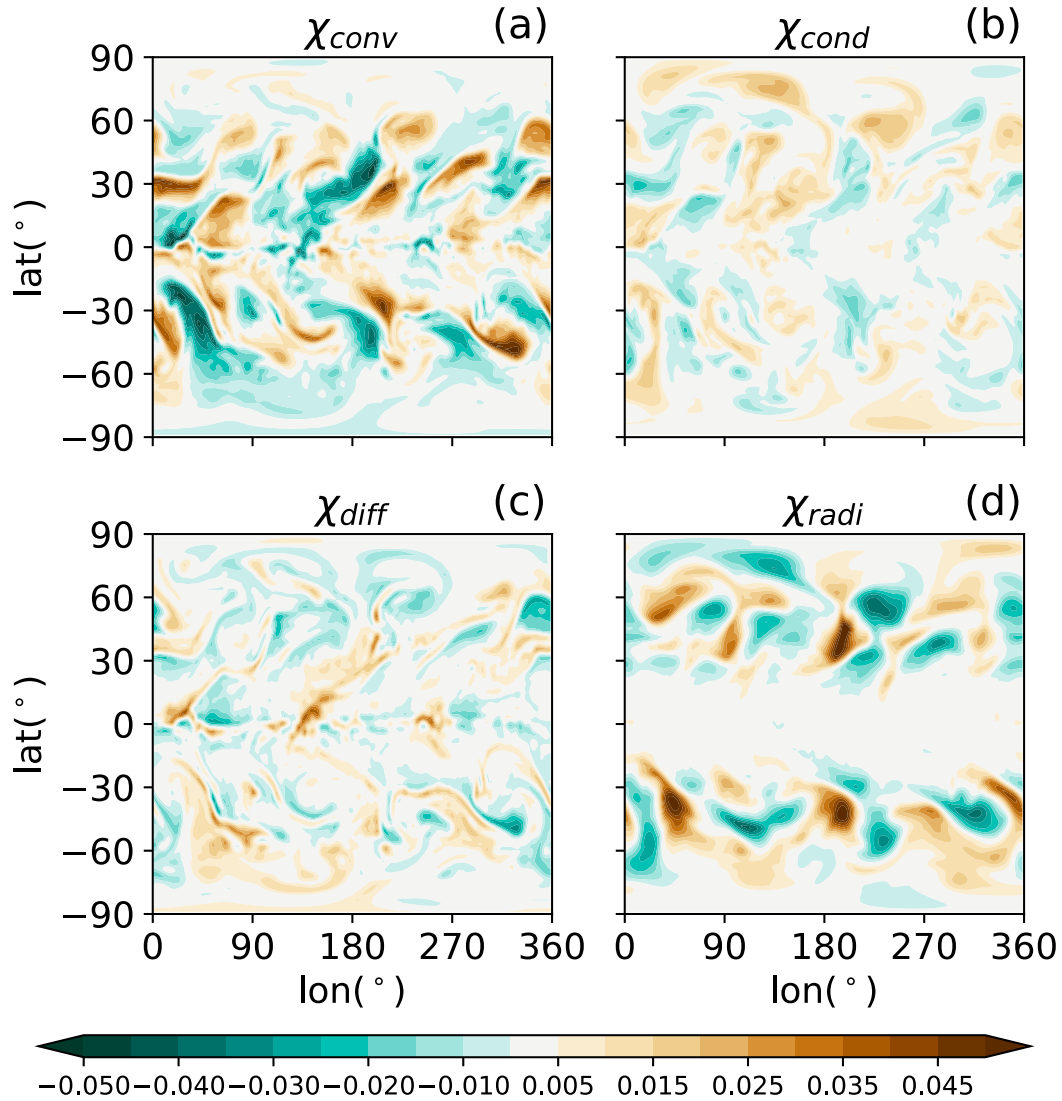


FIG. 6. (a) Representative snapshot of the vertically integrated χ'_{conv} . (b)–(d) As in (a), for χ'_{cond} , χ'_{diff} , and χ'_{radi} .

$$\text{var}(\theta_i) = \sum_{i=1}^{N_S} \sum_{j=1}^{N_S} \text{cov}(\theta_i, \theta_j) = \sum_{i=1}^{N_S} \left[\text{var}(\theta_i) + \sum_{j \neq i} \text{cov}(\theta_i, \theta_j) \right], \quad (27)$$

where $\text{cov}(\theta_i, \theta_j) \equiv \overline{\theta'_i \theta'_j}$ and $\text{var}(\theta_i) \equiv \text{cov}(\theta_i, \theta_i)$. The decomposition formally involves 10 terms; representative results from the decomposition are shown in Fig. 7.

The greatest variability in θ_{conv} is in the tropical lower troposphere (Fig. 7a), reflecting variability in convection near the surface and the mixing of high- θ_{conv} air masses from the free troposphere into the boundary layer. There is also strong variability that extends through the subtropics and into the midlatitudes. This variability might be associated with variability near the source and variability in the transport.

Variability in θ_{cond} (Fig. 7b) is much smaller than in θ_{conv} . It is greatest at the subtropical edge of the Hadley cell, the midlatitude upper troposphere, and the midlatitude near

surface. We note that the greatest variability in the subtropics is not near regions of large Q_{cond}^+ (Fig. 3b), again highlighting the role of transport and dynamics in creating variability in the heat tags.

In contrast to θ_{conv} and θ_{cond} , θ_{diff} appears to be locally controlled in the boundary layer; variability is greatest where most of the tag is produced (Figs. 7c, 3c). This could be due to the alternating pattern of Q_{diff}^+ and Q_{diff}^- (Figs. 3c,f). As θ_{diff} leaves the boundary layer it passes through a region of high Q_{diff}^- , which removes it from the atmosphere, and variability in this process seems to be reflected in Fig. 7c.

In the troposphere, these individual tag variances are much larger than, and have a spatial structure distinct from, the total variance of θ (Fig. 8a). This reflects compensation (large negative covariances) between the tags that is summarized by showing the covariance of the most variable tropospheric tag, θ_{conv} and the sum of the other tropospheric tags, θ_{cond} and θ_{diff} .

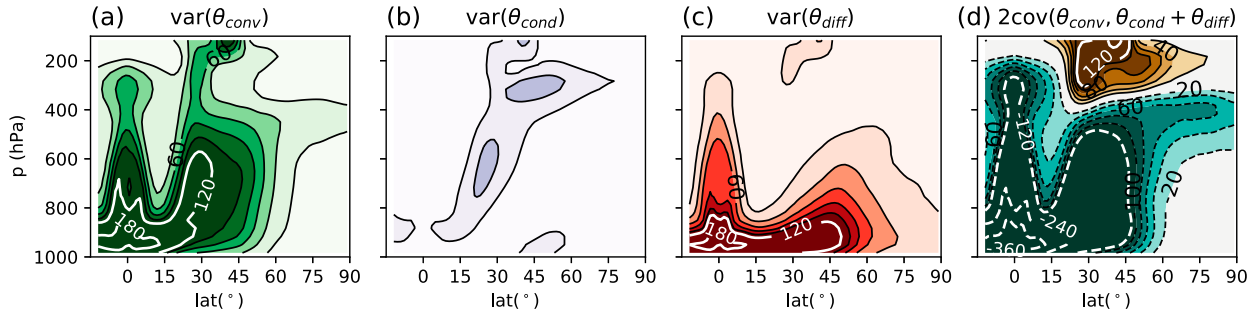


FIG. 7. (a) Zonal mean, climatological mean variance of θ_{conv} (contour interval: 20 K^2). (b)–(c) As in (a), but for θ_{cond} and θ_{diff} . (d) Two times the covariance between θ_{conv} and θ_{cond} and θ_{diff} . Extra contours are in white.

in Fig. 7d. The compensation is most obvious in the deep tropics where the large variances from θ_{conv} and θ_{diff} are almost perfectly cancelled by twice the covariance between the tropospheric heat tags [the factor of 2 is introduced to compare the variance terms to the covariance terms in the double sum in Eq. (27)].

While the covariance is negative throughout the troposphere, in the stratosphere there is positive covariance between all of the tropospheric tags (as partially shown in Fig. 7d). The variance of θ_{radi} is much greater than the variance of θ in the stratosphere (not shown), and has large negative covariability with the tropospheric tags in this region, in contrast to the positive covariability of the tropospheric tags in this region. We therefore interpret the positive covariability of the tropospheric tags in the stratosphere as being indicative of intrusions of tropospheric air into the stratosphere, carrying into the stratosphere air that is enriched with a mixture of tropospheric tags.

A complementary perspective on the variance analysis of (27) is provided by

$$\text{var}(\theta) = \sum_{i=1}^{N_s} \text{cov}(\theta_i, \theta), \quad (28)$$

for which each $\text{cov}(\theta_i, \theta)$ (Fig. 8) indicates how tag i contributes to total θ variance (Fig. 8a). In this analysis, the dominance of the contribution of θ_{conv} (Fig. 8b) in the troposphere is evident. This reflects how variability in tropical convective heating is communicated, via transport, into the midlatitudes, and dominates variability there. This contribution accounts for the main tropospheric structure of $\text{var}(\theta)$ equatorward of 50° (Fig. 8a); contributions from the other tags are of mixed sign and comparatively weak in the troposphere. This shows that, for this model, high- θ_{conv} tropical air masses are responsible for the variability of temperature in the midlatitudes.

Poleward of 65° , $\text{cov}(\theta_{conv}, \theta)$ is important in the upper troposphere, but $\text{cov}(\theta_{diff}, \theta)$ is the dominant contribution to $\text{var}(\theta)$ (Fig. 8c) in the lower troposphere. Near the surface the air is isolated from the rest of the atmosphere (Orbe et al. 2015), while above the planetary boundary layer in the polar region the variability of θ is still dominated by $\text{cov}(\theta_{conv}, \theta)$. This suggests that although local dynamics are important for the variability of the surface temperature, the variability of the

mid- and upper troposphere in polar regions is controlled by remote contributions (Fajber et al. 2018).

In the stratosphere, the dominant contribution to stratospheric θ variance is θ_{radi} (not shown). This is suggested by Fig. 6 and consistent with the results and analysis of Fig. 7 discussed above.

e. Airmass analysis

While the covariance analysis of the previous subsection is useful for describing how the variability of the tags relates to the variability of θ , it is hard to compare between different regions, since θ and $\text{var}(\theta)$ varies greatly with latitude and pressure. However, $0 < \chi_i < 1$, and so χ_i can be compared between different regions more easily. In this subsection we therefore use the joint probability distribution function (pdf) of χ_i to characterize the variation between the tags and show that they can be used to characterize different air masses in the atmosphere.

Airmass characteristics can be inferred from the mass-weighted joint pdfs of the tag fractions. Figure 9 shows the joint pdf of χ_{cond} and χ_{conv} for the tropical midtroposphere (Fig. 9a), the extratropical midtroposphere (Fig. 9b), the tropical lower troposphere (Fig. 9c), and the extratropical lower troposphere (Fig. 9d). Notice that almost the entire troposphere occupies the range $0.20 < \chi_{conv} < 0.50$ and $0.2 < \chi_{cond} < 0.40$, which bracket the well-mixed estimates (Table 3). For over 95% of the mass of the regions considered here, $\chi_{radi} < 0.05$ (not shown). In these regions, then, the diffusive tag is constrained by the two other tags via [Eq. (12)]:

$$\chi_{diff} \approx 1 - \chi_{conv} - \chi_{cond}. \quad (29)$$

To aid in our analysis, we will analyze two populations, represented by the lines

$$\chi_{cond}^1 = \chi_{conv}^1 + 0.10 \Rightarrow \chi_{diff}^1 \approx 0.90 - 2\chi_{conv}^1$$

(shown in Fig. 9a) and

$$\chi_{cond}^2 = -\frac{2}{3}\chi_{conv}^2 + 0.56 \Rightarrow \chi_{diff}^2 \approx 0.44 - \frac{1}{3}\chi_{conv}^2$$

(shown in Fig. 9d). The relationships between χ_{conv} and the other two tropospheric heat tag fractions for these populations

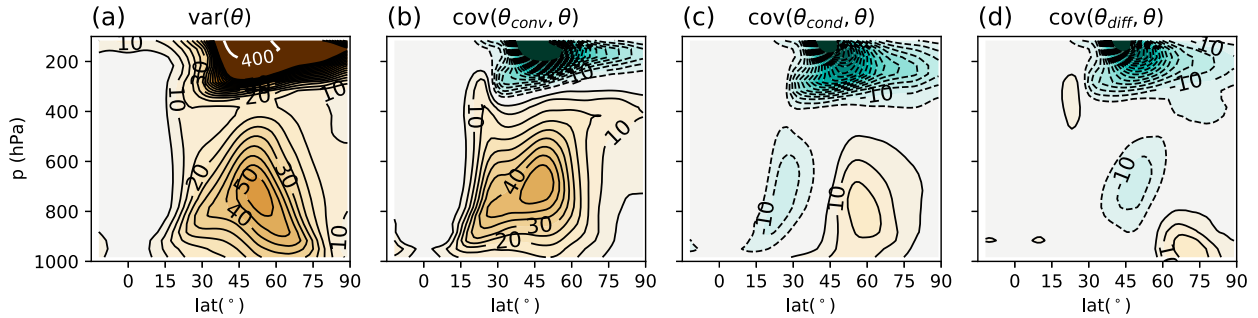


FIG. 8. (a) Zonal mean, climatological mean variance of θ (contour interval: 5 K^2). (b) The zonal mean, climatological mean covariance between θ_{conv} and θ (contour interval: 5 K^2). (b)–(d) As in (a), but for θ_{cond} and θ_{diff} . Extra contours are in white.

are sketched in Fig. 9f. We note that these relationships are for illustrative purposes and do not represent a rigorous separation of the data into distinct populations.

The first population is found mainly in the tropics. It is characterized by a long tail of high χ_{conv} values being replaced by χ_{cond} and, in a ratio of 2:1, by χ_{diff} . This air features high values of χ_{conv} in the upper and mid-tropical troposphere, and is then mixed with air of lower χ_{conv} . Integrating the pdfs over the region $\chi_{\text{conv}} > 0.30$, an approximate boundary for this population, we find that this population contains about 33% of the mass of the atmosphere.

The second population is mainly found near the surface. Integrating the pdfs over the region $\chi_{\text{conv}} \leq 0.26$ we find that this population makes up about 41% of the atmosphere. It is characterized by high χ_{diff} values compared to the first population. The contributions of χ_{conv} and χ_{cond} increase at the same rate, although χ_{cond} is higher. This population lies near or in the planetary boundary layer.

Between the populations, in the region $0.25 < \chi_{\text{conv}} < 0.30$ the air has $\chi_{\text{cond}} \approx 0.36$. We interpret the air in this region as resulting from the mixing of the two different populations. This mixed population is found primarily in the extratropical mid-troposphere (Fig. 9b), where there are no diabatic sources in the atmosphere. In this region the fractionation between χ_{conv} and χ_{cond} is set by the mixing of air masses created in different environments. The mixed population also exists in the tropical mid- and lower troposphere. This is the signature of air mixing from either the surface or polar latitudes into the tropics. Integrating the pdfs over the region $0.25 < \chi_{\text{cond}} < 0.30$ we find that this mixed population makes up about 26% of the mass of the atmosphere.

Taken together, this diagnostic suggests thinking of the troposphere as composed of an air mass with high χ_{conv} values (intermediate χ_{diff} and low χ_{cond} values), residing in the tropics, and an air mass with low χ_{conv} values (intermediate χ_{cond} and high χ_{diff} values), residing near the surface. The air mass in the lower tropical troposphere and extratropical midtroposphere come from the mixing of these two air masses.

f. Vertically integrated transport

The vertically integrated total, mean, and eddy, transport of a given tag are given by

$$H_i^T = 2\pi a \cos\phi \int \overline{v\theta}_i \frac{dp}{g},$$

$$H_i^M = 2\pi a \cos\phi \int \overline{v\theta}_i \frac{dp}{g},$$

$$H_i^E = 2\pi a \cos\phi \int \overline{v\theta}_i' \frac{dp}{g},$$

respectively. Since the expressions are linear in θ , the transport of θ is the sum of the tag transports: $H_\theta^T = \sum H_i^T$. Similar expressions hold for H_θ^M and H_θ^E . We also define the transports of $L_\alpha q$, denoted H_Q , which can be added to H_θ to find the transport of θ_e : $H_{\theta_e} = H_Q + H_\theta$

Total θ transport (Fig. 10f shows the tropospheric contribution to H_θ^T ; H_{radi}^T is small but composed of large cancellations, as discussed below) is dominated by a poleward flux of magnitude 6 PW from H_{conv}^T (solid curve in Fig. 10a) from the tropics into the midlatitudes. In the tropics, this is dominated by the Hadley circulation term H_{conv}^M (dotted line in Fig. 10a) which is then taken over by eddy transport H_{conv}^E (dashed line in Fig. 10b) in the extratropics. Air tagged as convectively generated is transported out of the deep tropics through the Hadley cell, which is then transported further poleward by the midlatitude eddies, explicitly demonstrating the relation implied by Trenberth and Stepaniak (2003).

The remaining heat tags are responsible for relatively less θ transport. The θ_{cond} transport H_{cond}^T is dominated by H_{cond}^E , which is negative equatorward of 45° and positive poleward of 45° (Fig. 10b). This suggests that the eddies transport θ_{cond} away from the region where it is produced (Fig. 3b). H_{cond}^M is relatively weak in comparison. The relatively weak transport of the diffusive tag by the mean circulation, H_{diff}^M (Fig. 10c), is opposite in sign to that of H_{conv}^M , simply because θ_{conv} is amplified in the upper troposphere and θ_{diff} is amplified at the surface (Figs. 4a,d). Similar to H_{cond}^E , H_{diff}^E diffuses energy away from the maximum of the source of θ_{diff} , which is around 60° .

Even though the tag with a tropical source θ_{conv} plays the largest role globally, in the high latitudes, the tags with midlatitude sources θ_{cond} and θ_{diff} become more important. At 50° $(H_{\text{cond}}^T + H_{\text{diff}}^T)/H_\theta^T \approx 0.4$, but as latitude increases to poleward of 65° , $(H_{\text{cond}}^T + H_{\text{diff}}^T)/H_\theta^T \approx 0.65$. Thus, heat transport from $\theta_{\text{cond}} + \theta_{\text{diff}}$ is important for maintaining the heat content of the

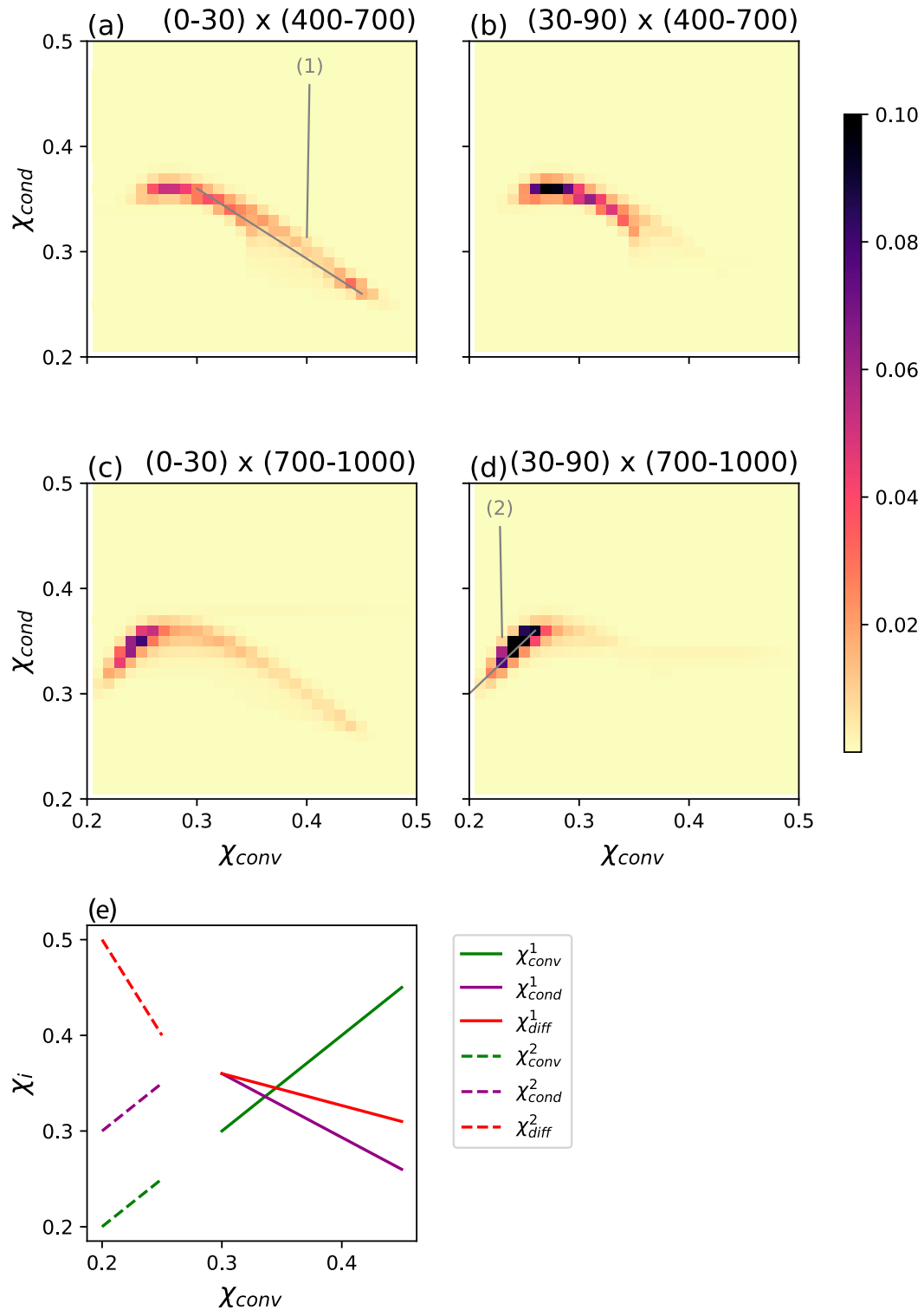


FIG. 9. (a) Double tag pdfs for $0^\circ\text{--}30^\circ$ latitude and 400–700 hPa, or the tropical midtroposphere. (b) As in (a), but for the extratropical midtroposphere. (c) As in (a), but for the tropical lower troposphere. (d) As in (a), but for the extratropical lower troposphere. The solid gray lines in (a) and (d) describe two different populations of points, as defined and discussed in the text. (e) The values of χ_{conv} , χ_{cond} , and χ_{diff} [implied by Eq. (29)] for the gray lines shown in (a) and (b).

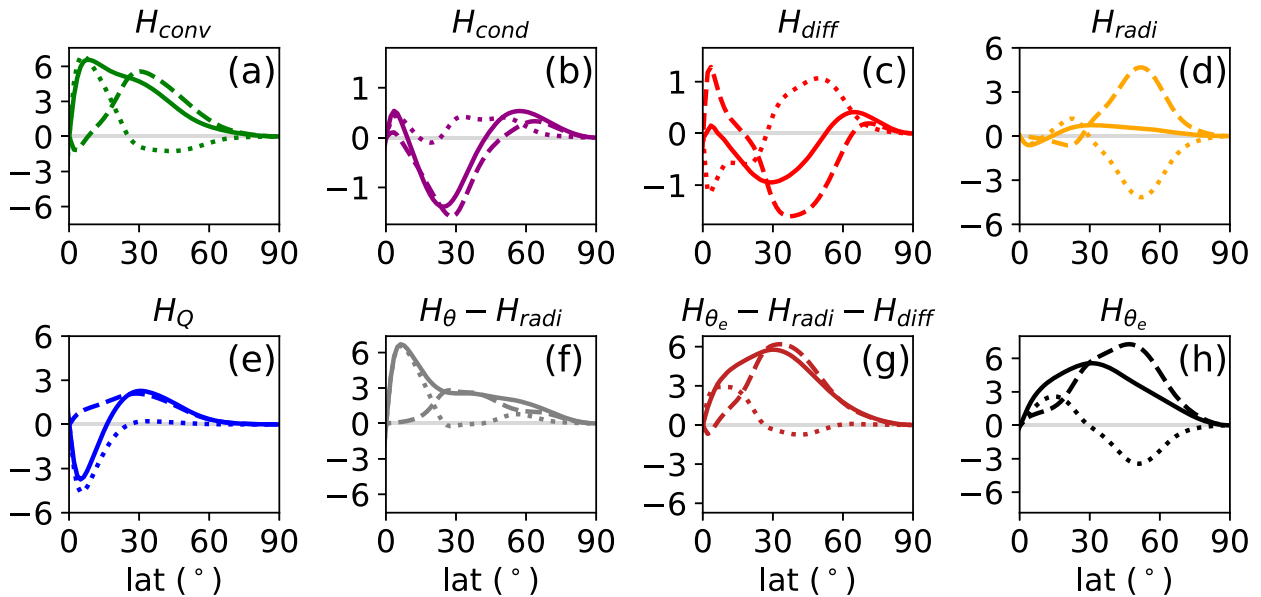


FIG. 10. Vertically integrated transport for (a)–(d) the heat tags, (e) $L_v q$, (f) $\theta - \theta_{\text{radi}}$ (see text for details), (g) $\theta_e - \theta_{\text{radi}}$, and (h) θ_e . The solid line is H^T , the dotted line is H^M , and the dashed line is H^E . The units for all are PW.

polar atmosphere, even though it is relatively small in other regions. While these numbers no doubt depend on the model parameterizations used here, the broader point is that there is a connection between midlatitude diabatic processes and heat transport to the polar regions, despite the dominance of the tropical diabatic processes in global heat transport.

The total transport of the radiative tag, H_{radi}^T (Fig. 10d), is a small residual between the sum of large equatorward H_{radi}^M transport and a large and poleward H_{radi}^E (comparing the dashed and dotted lines in Figs. 10a–c). This causes a large cancellation between H_{θ}^M and H_{θ}^E in the midlatitudes, which does not occur in H_{θ}^T . Indeed $H_{\theta}^T - H_{\text{radi}}^T$ (Fig. 10f) does not show the same cancellation between mean and eddy components.

Because radiative tag is primarily produced in the stratosphere, its production and transport are strongly influenced by the representation of the stratospheric circulation in this low-top model. One issue of concern is that this version of the model makes use of the default sponge layer formulation based on Rayleigh drag applied to the zonal winds, which can readily lead to spurious circulations in the stratosphere (Shepherd and Shaw 2004). Since H_{radi}^T is still required to be small by the diabatic tendencies in the stratosphere, a large compensatory H_{radi}^E is developed. Capturing heat tag processes within a model with a more realistic stratospheric representation merits further investigation. This being said, we note that diagnosing the midlatitude compensation in H_{θ}^M and H_{θ}^E as a result of the stratospheric transport was aided by having the heat tags. This highlights the potential of the heat tags to aid understanding of atmospheric heat transport and diagnosing unrealistic aspects of simulated heat transport.

The large transport of $H_{\theta}^M - H_{\theta}^E$ in the tropics is opposed by H_Q^M (dotted line in Fig. 10e). These transports are connected to the two branches of the Hadley cell; the upper branch exports

θ from the tropics into the extratropics, and the lower branch transports moisture equatorward. The eddy moisture transport H_Q^E (dashed line in Fig. 10e) is poleward throughout the atmosphere, peaking in the tropics.

Noting that H_{diff}^T and H_{radi}^T are small, we compare $H_{\theta_e}^T - H_{\text{diff}}^T - H_{\text{radi}}^T$ (Fig. 10g) and $H_{\theta_e}^T$ (Fig. 10h). Since $H_{\theta_e}^T - H_{\text{diff}}^T - H_{\text{radi}}^T = H_Q^T + H_{\text{conv}}^T + H_{\text{cond}}^T$, this transport is also the heat transport related to moisture and latent heating. The difference in the partitioning between mean and eddy transport in $H_{\theta_e}^T$ and $H_{\theta_e}^T - H_{\text{diff}}^T - H_{\text{radi}}^T$ is largely due to the compensations in H_{radi}^T . The total transport of θ_e is largely due to $H_{\theta_e}^T - H_{\text{diff}}^T - H_{\text{radi}}^T$; in midlatitudes it is largely dominated by the eddy transport while in the tropics the partitioning is almost evenly split between the mean and eddy transport. The large contribution of $H_{\theta_e}^T - H_{\text{diff}}^T - H_{\text{radi}}^T$ to $H_{\theta_e}^T$ shows that moist processes dominate the total heat transport of the atmosphere.

4. Discussion and conclusions

Airmass information using numerical transport of tracers provides an effective manner to link diabatic processes across separated regions of the atmosphere. The heat tagging method introduced here is well suited to this purpose in climate simulations because the tags are nonnegative, finite, and partition the total dry heat content of the atmosphere by construction. Remote linkages in the atmosphere through heat transport can be inferred from Figs. 3 and 4: although the sources of heat in the atmosphere are relatively well localized, the tags corresponding to heating are spread throughout the atmosphere. At least in the present model, in the polar column the heat produced in tropical convection makes as large a contribution to the total heat as the heat produced by surface sensible heating, even though the tropics are over 6600 km away. Although the result appears reasonable a posteriori it

could not have been quantified, a priori, without using a method such as heat tagging.

An important advance of using our method over solely using local diabatic tendencies is that it allows us to diagnose the remote effects of these tendencies. Local latent heating determines the local balance between heating, cooling, and transport (e.g., Trenberth and Stepaniak 2003), and modifies local dynamics (e.g., Schneider et al. 2010). By combining the distribution of latent heating with the mass transport of the global circulation we can now quantitatively partition the heat content of remote regions to latent heating and other diabatic processes.

The heat tags quantify the role of latent heating in maintaining the heat content of the atmosphere, demonstrating the importance of the hydrological cycle to atmospheric heat content. The tags related to latent heating make up 60%–80% of the heat content in the free troposphere, including in the polar troposphere where there is negligible latent heating. This is despite the fact that water vapor makes up less than 2% of the total heat content in the atmosphere. The difference in time scales between the condensation, which removes water vapor from the atmosphere, and longwave cooling, which removes the extra heat added by latent heating, explains this difference. In other words, it is the cycling of water vapor through the atmosphere, not the amount of water vapor in the atmosphere, which controls the contribution of latent heating to the atmospheric heat content. Future evaluation of how the hydrologic cycle controls climate thus could be enriched by using heat tags to analyze not only the local effects of water vapor or condensation, but also how this heat content is transported to and affects remote regions.

Since convective heating is greatest in the tropics and radiative heating is greatest in stratosphere, we have interpreted these tags as containing regional information. However, there is no guarantee that diabatic heating needs to be regionally isolated as it is in our model, and indeed separate numerical experiments (not shown) suggest that the regional structure can be strongly influenced by choices in physical parameterizations. In another approach, heat tags might be subdivided to be sourced from different spatial regions similar to water tagging (Singh et al. 2016; Dyer et al. 2017). This is challenging with our current model set up, since these tags can have sharp gradients which our spectral transport scheme has difficulty resolving. However, there is nothing inherent in our method that prevents further regional decomposition.

In any case, for the current model configuration, we have learned that 1) only a small fraction of the standard deviation of θ is attributable to sensible heating, and this is mostly confined to the polar near surface, and 2) in the midlatitudes the majority of the variability arises from tropical latent heating. To correctly capture the temperature variability in the midlatitudes our results suggest that it is important to accurately capture the heat content of tropical air masses as well as diabatic heating in the midlatitudes. Furthermore, polar variability also appears to hinge on the long-range transport of the atmosphere as well as accurately representing local processes.

We have presented only a limited picture of dynamical insight that could be gained within this framework. For example,

through a time-lagged analysis we could study how convectively warmed air masses exported out of the tropics might influence midlatitude weather systems. Another interesting class of dynamics yet to be explored is tropical wave phenomenon, in which latent heating generates a wave which triggers convection in another location in the tropics. Since the heat content in one region is being generated through local latent heating (triggered by remote latent heating), and not advection of warm air mass, this will not be captured directly using our approach. Partitioning diabatic process tags into multiple tropical and midlatitude regions, and examining their time-lagged covariance, might provide deeper insight into these dynamical problems, particularly when combined with atmospheric wave diagnostics.

This work would benefit by being systematically extended to more complex models in the hierarchy, beyond this simplified aquaplanet model which lacks a seasonal cycle, land, cloud–radiative interactions, etc. In particular, the seasonal cycle plays an important role in regulating transport from the midlatitudes to the Arctic, and introducing land and sea ice would introduce stationary waves, which accomplish a large fraction of the transport in the subtropics (Holzer 1999; Holzer and Boer 2001). Since the convection parameterization of this model does not simulate a mass flux, we cannot explicitly capture the convectively triggered mass transport, which plays an important role in transporting tracers from the boundary layer to the upper troposphere in the deep tropics (Erukhimova and Bowman 2006), and which would alter the distribution of heat tags in the tropics. Applying heat tagging to models with less idealized insolation and boundary conditions will bring insights into these processes and the role that long-range transport plays in climate variability and change.

Acknowledgments. We thank editor William Boos and two other anonymous reviewers for their thoughtful comments on an earlier draft of the paper. RF acknowledges funding from NSERC Canada through a CGS-D award and the U.S. Department of Energy through Grant DE-SC001940. Computations were performed on the Niagara supercomputer at the SciNet HPC Consortium.

Data availability statement. The data and modifications to the model code are available from the author on request.

REFERENCES

- Dyer, E. L., D. B. Jones, J. Nusbaumer, H. Li, O. Collins, G. Vettoretti, and D. Noone, 2017: Congo basin precipitation: Assessing seasonality, regional interactions, and sources of moisture. *J. Geophys. Res.*, **122**, 6882–6898, <https://doi.org/10.1002/2016JD026240>.
- Erukhimova, T., and K. P. Bowman, 2006: Role of convection in global-scale transport in the troposphere. *J. Geophys. Res.*, **111**, D03105, <https://doi.org/10.1029/2005JD006006>.
- Fajber, R., P. J. Kushner, and F. Laliberté, 2018: Influence of midlatitude surface thermal anomalies on the polar mid-troposphere in an idealized moist model. *J. Atmos. Sci.*, **75**, 1089–1104, <https://doi.org/10.1175/JAS-D-17-0283.1>.
- Fisher, J. A., L. Murray, D. Jones, and N. M. Deutscher, 2017: Improved method for linear carbon monoxide simulation and

- source attribution in atmospheric chemistry models illustrated using GEOS-Chem v9. *Geosci. Model Dev.*, **10**, 4129–4144, <https://doi.org/10.5194/gmd-10-4129-2017>.
- Frierson, D. M., 2007: The dynamics of idealized convection schemes and their effect on the zonally averaged tropical circulation. *J. Atmos. Sci.*, **64**, 1959–1976, <https://doi.org/10.1175/JAS3935.1>.
- , I. M. Held, and P. Zurita-Gotor, 2006: A gray-radiation aquaplanet moist GCM. Part I: Static stability and eddy scale. *J. Atmos. Sci.*, **63**, 2548–2566, <https://doi.org/10.1175/JAS3753.1>.
- Galewsky, J., A. Sobel, and I. Held, 2005: Diagnosis of subtropical humidity dynamics using tracers of last saturation. *J. Atmos. Sci.*, **62**, 3353–3367, <https://doi.org/10.1175/JAS3533.1>.
- Hall, T. M., and R. A. Plumb, 1994: Age as a diagnostic of stratospheric transport. *J. Geophys. Res.*, **99**, 1059–1070, <https://doi.org/10.1029/93JD03192>.
- Holzer, M., 1999: Analysis of passive tracer transport as modeled by an atmospheric general circulation model. *J. Climate*, **12**, 1659–1684, [https://doi.org/10.1175/1520-0442\(1999\)012<1659:AOPTTA>2.0.CO;2](https://doi.org/10.1175/1520-0442(1999)012<1659:AOPTTA>2.0.CO;2).
- , and G. J. Boer, 2001: Simulated changes in atmospheric transport climate. *J. Climate*, **14**, 4398–4420, [https://doi.org/10.1175/1520-0442\(2001\)014<4398:SCIATC>2.0.CO;2](https://doi.org/10.1175/1520-0442(2001)014<4398:SCIATC>2.0.CO;2).
- , and T. M. Hall, 2008: Tropospheric transport climate partitioned by surface origin and transit time. *J. Geophys. Res.*, **113**, D08104, <https://doi.org/10.1029/2007JD009115>.
- Ling, J., and C. Zhang, 2013: Diabatic heating profiles in recent global reanalyses. *J. Climate*, **26**, 3307–3325, <https://doi.org/10.1175/JCLI-D-12-00384.1>.
- Martínez-Alvarado, O., and R. S. Plant, 2014: Parametrized diabatic processes in numerical simulations of an extratropical cyclone. *Quart. J. Roy. Meteor. Soc.*, **140**, 1742–1755, <https://doi.org/10.1002/qj.2254>.
- O’Gorman, P. A., and T. Schneider, 2008: The hydrological cycle over a wide range of climates simulated with an idealized GCM. *J. Climate*, **21**, 3815–3832, <https://doi.org/10.1175/2007JCLI2065.1>.
- Orbe, C., M. Holzer, L. M. Polvani, and D. Waugh, 2013: Air-mass origin as a diagnostic of tropospheric transport. *J. Geophys. Res.*, **118**, 1459–1470, <https://doi.org/10.1002/jgrd.50133>.
- , P. A. Newman, D. W. Waugh, M. Holzer, L. D. Oman, F. Li, and L. M. Polvani, 2015: Air-mass origin in the Arctic. Part I: Seasonality. *J. Climate*, **28**, 4997–5014, <https://doi.org/10.1175/JCLI-D-14-00720.1>.
- , D. W. Waugh, P. A. Newman, and S. Steenrod, 2016: The transit-time distribution from the Northern Hemisphere midlatitude surface. *J. Atmos. Sci.*, **73**, 3785–3802, <https://doi.org/10.1175/JAS-D-15-0289.1>.
- Pauluis, O., A. Czaja, and R. Korty, 2008: The global atmospheric circulation on moist isentropes. *Science*, **321**, 1075–1078, <https://doi.org/10.1126/science.1159649>.
- , —, and —, 2010: The global atmospheric circulation in moist isentropic coordinates. *J. Climate*, **23**, 3077–3093, <https://doi.org/10.1175/2009JCLI2789.1>.
- Peixoto, J. P., and A. H. Oort, 1992: *Physics of Climate*. American Institute of Physics, 520 pp.
- Pfahl, S., C. Schwierz, M. Croci-Maspoli, C. M. Grams, and H. Wernli, 2015: Importance of latent heat release in ascending air streams for atmospheric blocking. *Nat. Geosci.*, **8**, 610–614, <https://doi.org/10.1038/ngeo2487>.
- Rasch, P. J., and D. L. Williamson, 1990: Computational aspects of moisture transport in global models of the atmosphere. *Quart. J. Roy. Meteor. Soc.*, **116**, 1071–1090, <https://doi.org/10.1002/qj.49711649504>.
- Schemm, S., H. Wernli, and L. Papritz, 2013: Warm conveyor belts in idealized moist baroclinic wave simulations. *J. Atmos. Sci.*, **70**, 627–652, <https://doi.org/10.1175/JAS-D-12-0147.1>.
- Schneider, T., P. A. O’Gorman, and X. J. Levine, 2010: Water vapor and the dynamics of climate changes. *Rev. Geophys.*, **48**, RG3001, <https://doi.org/10.1029/2009RG000302>.
- Shaw, T. A., and O. Pauluis, 2012: Tropical and subtropical meridional latent heat transports by disturbances to the zonal mean and their role in the general circulation. *J. Atmos. Sci.*, **69**, 1872–1889, <https://doi.org/10.1175/JAS-D-11-0236.1>.
- Shepherd, T. G., and T. A. Shaw, 2004: The angular momentum constraint on climate sensitivity and downward influence in the middle atmosphere. *J. Atmos. Sci.*, **61**, 2899–2908, <https://doi.org/10.1175/JAS-3295.1>.
- Singh, H. A., C. M. Bitz, J. Nusbaumer, and D. C. Noone, 2016: A mathematical framework for analysis of water tracers: Part 1: Development of theory and application to the preindustrial mean state. *J. Adv. Model. Earth Syst.*, **8**, 991–1013, <https://doi.org/10.1002/2016MS000649>.
- Sodemann, H., H. Wernli, and C. Schwierz, 2009: Sources of water vapour contributing to the Elbe flood in August 2002—A tagging study in a mesoscale model. *Quart. J. Roy. Meteor. Soc.*, **135**, 205–223, <https://doi.org/10.1002/qj.374>.
- Trenberth, K. E., and D. P. Stepaniak, 2003: Seamless poleward atmospheric energy transports and implications for the Hadley circulation. *J. Climate*, **16**, 3706–3722, [https://doi.org/10.1175/1520-0442\(2003\)016<3706:SPAETA>2.0.CO;2](https://doi.org/10.1175/1520-0442(2003)016<3706:SPAETA>2.0.CO;2).
- Vallis, G. K., and Coauthors, 2018: Isca, v1.0: A framework for the global modelling of the atmospheres of Earth and other planets at varying levels of complexity. *Geosci. Model Dev.*, **11**, 843–859, <https://doi.org/10.5194/gmd-11-843-2018>.
- Wang, Y., Y. Zhang, J. Hao, and M. Luo, 2011: Seasonal and spatial variability of surface ozone over China: Contributions from background and domestic pollution. *Atmos. Chem. Phys.*, **11**, 3511–3525, <https://doi.org/10.5194/acp-11-3511-2011>.
- Waugh, D., and T. Hall, 2002: Age of stratospheric air: Theory, observations, and models. *Rev. Geophys.*, **40**, 1010, <https://doi.org/10.1029/2000RG000101>.
- Zhang, K., W. J. Randel, and R. Fu, 2017: Relationships between outgoing longwave radiation and diabatic heating in reanalyses. *Climate Dyn.*, **49**, 2911–2929, <https://doi.org/10.1007/s00382-016-3501-0>.